

NORTHWESTERN UNIVERSITY

**A Search for Dark Matter Produced in Association with $t\bar{t}$ at $\sqrt{s}=13$ TeV in the
Dilepton Final State with the CMS Experiment**

A DISSERTATION

**SUBMITTED TO THE GRADUATE SCHOOL
IN PARTIAL FULFILLMENT OF THE REQUIREMENTS**

for the degree

DOCTOR OF PHILOSOPHY

Field of Physics and Astronomy

By

Stanislava Lubomirova Sevova

EVANSTON, ILLINOIS

June 2018

Abstract

4.5 years of POOP!

Declaration

I haz dun most of dis werk.

Stanislava Sevova

Acknowledgements

H8rz gonna h8.

Preface

This thesis describes my research on various aspects of the CMS particle physics program, centred around the CMS detector and LHC accelerator at CERN in Geneva.

For this example, I'll just mention Chapter ?? and Chapter ??.

Contents

1. Dark matter: Beyond the Standard Model	1
1.0.1. Introduction to dark matter	2
1.0.2. Dark matter detection	3
1.0.3. The Standard Model	3
2. The CMS experiment	5
2.1. The LHC	5
2.2. The CMS experiment	5
3. Event Reconstruction	11
3.1. Leptons	11
3.1.1. Muons	12
3.1.2. Electrons	15
3.2. Jets	19
3.2.1. b jet tagging	21
3.3. Missing transverse energy	23
3.4. Event Selection	26
3.4.1. The $M_{T2}^{\ell\ell}$ variable	27
4. Background processes	31
4.1. $t\bar{t}(2\ell)$	32

4.2. Drell-Yan	33
4.2.1. The $R_{\text{in/out}}$ method	34
4.3. $t\bar{t} + V$, diboson processes, and single top	42
4.4. Fake lepton background	42
A. Pointless extras	45
A.1. Like, duh	45
A.2. $y = \alpha x^2$	46
Bibliography	49
List of figures	51
List of tables	53

Chapter 1.

Dark matter: Beyond the Standard Model

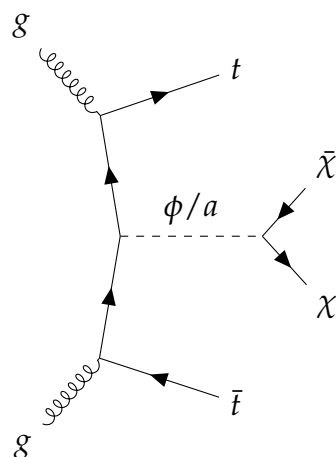
The Standard Model (SM) of particle physics, albeit a successful theory encoding the properties of elementary particles and their interactions, nonetheless has some shortcomings. For one, cosmological and astrophysical observations supply compelling evidence [1–3] for the existence of dark matter (DM), a piece of the astro-particle physics puzzle which does not fit together with the SM. In Sec. 1.0.1, evidence and motivations for the hunt for DM are briefly detailed, while in Sec. 1.0.2 the main modes of DM detection are outlined, with particular emphasis on collider detection. In Sec. 1.0.3, the connection between the SM and DM is presented with particular emphasis on beyond the Standard Model (BSM) simplified DM models currently being probed at general-purpose detectors at the Large Hadron Collider (LHC) in Geneva, Switzerland.

1.0.1. Introduction to dark matter

Observations at all scales, from smaller dwarf galaxies to large cosmological scales point to the existence of more matter than is reconcilable with the amount of visible matter in our universe. This was first postulated by Swiss physicist Fritz Zwicky in 1933 whilst observing the Coma cluster. Zwicky's observations pointed to the need for approximately 10 times the mass as observed from the visible light of the cluster to ensure the gravitational bounding of individual galaxies within the cluster itself. Subsequently Vera Rubin's research in the 1970's revealed the flat dependence of v , the galactic rotation velocity, as a function of the radius r beyond the visible galactic disk demonstrating that mass extends past the visible disk. By the 1980's the majority of the astrophysical community was convinced that a substantial amount of invisible matter existed in the universe.

Studies of the large scale structure of the universe have provided clues as to the nature of dark matter. Just as on the small scale, ordinary visible matter consists of protons, electrons, neutrons, or groups of atoms held together by the electromagnetic force, similarly groups of stars are bound together by the gravitational force provided sufficiently massive in order to form galaxies, and galaxies form clusters, and so on. The observation that star ages within galaxies are on the order of 10 to 14 billion years old, and cluster formation is still under way serves to support the cold dark matter (CDM) hypothesis. In this case, DM comprises of rather massive, slow moving, and non-relativistic particles, which would stimulate the clumping of matter into small regions initially, eventually giving rise to larger scale structures. This bottom-up theory of structure formation is further supported by myriad computer simulations consisting of billions of dark matter particles confirming the CDM model yields large structures such as those observed by the Sloan Digital Sky Survey.

1.0.2. Dark matter detection



1.0.3. The Standard Model

Chapter 2.

The CMS experiment

2.1. The LHC

The Large Hadron Collider (LHC) at CERN is the most powerful particle accelerator in the world, located in the same tunnel as the Large Electron-Positron collider (LEP) [4]. The mandate of the LHC experimental program is two-fold: to probe the electroweak symmetry breaking mechanism via which particles in the Standard Model (SM) attain mass, and to extend the exploration of the energy frontier in search for new physics beyond the SM (BSM).

2.2. The CMS experiment

The CMS detector, described in detail in Ref. [5], is a multi-purpose apparatus designed to study high- p_T physics processes in proton-proton and heavy-ion collisions. A superconducting solenoid in its central region provides a magnetic field of 3.8 T parallel to the beam direction. Charged particle trajectories are measured by silicon

pixel and strip trackers, which cover a pseudorapidity region of $|\eta| < 2.5$. Surrounding the tracker volume are a lead-tungstate crystal electromagnetic calorimeter (ECAL) and a brass-and-scintillator hadron calorimeter (HCAL) surround the tracking volume, covering the region of $|\eta| < 3$. A steel and quartz-fiber Cherenkov forward hadron calorimeter extends the coverage to $|\eta| < 5$. The muon system consists of gas-ionization detectors embedded in the steel flux return yoke outside the solenoid, and covers the region with $|\eta| < 2.4$. The detector is designed to cover a 4π solid angle. The detector is illustrated in Figure 2.1, showing the overall scale of the experiment and the surrounding cavern structure.

The first level of the CMS trigger system is composed of custom hardware processors and designed to select the most interesting events in less than $4\ \mu\text{s}$, using information from the calorimeters and muon detectors. This system reduces the event rate from 40 MHz to approximately 100 kHz. The high-level trigger processor farm performs a coarse reconstruction of events selected by the first-level trigger, and applies additional selections to reduce the event rate to about 1 kHz for storage.

One of the main mandates of the CMS detector is to provide good resolution and reconstruction efficiency for charged particles emitted from LHC collisions in the inner tracker. Furthermore, the precise reconstruction of secondary vertices is imperative for the efficient identification of b-jets; b-jets being the only flavor jets expected in the dilepton channel $t\bar{t} + \chi\bar{\chi}$ signal final state topology. To achieve this, it is imperative for the positioning of tracker layers to be close to the interaction point of a collision, hence the first and last of the three pixel barrel layers are stationed at radii 4.4 cm to 10.4 cm. What follows these layers, are the four and six silicon strip layers comprising the Tracker Inner Barrel (TIB), and Tracker Outer Barrel (TOB), respectively.

The last TOB layer reaches an outward radius of 1.1 m from the beampipe. The barrel layers of both the pixel and strip systems are complimented by disk layers on either $\pm z$ position of the interaction point. There are two pixel disks on either side of the barrel layer, while there are three small disks and nine larger disks, known as the Tracker Inner Disks (TID) and Tracker EndCaps (TEC) respectively, which flank the strip barrel layers. A cross-sectional view of the tracker can be seen in Figure 2.2.

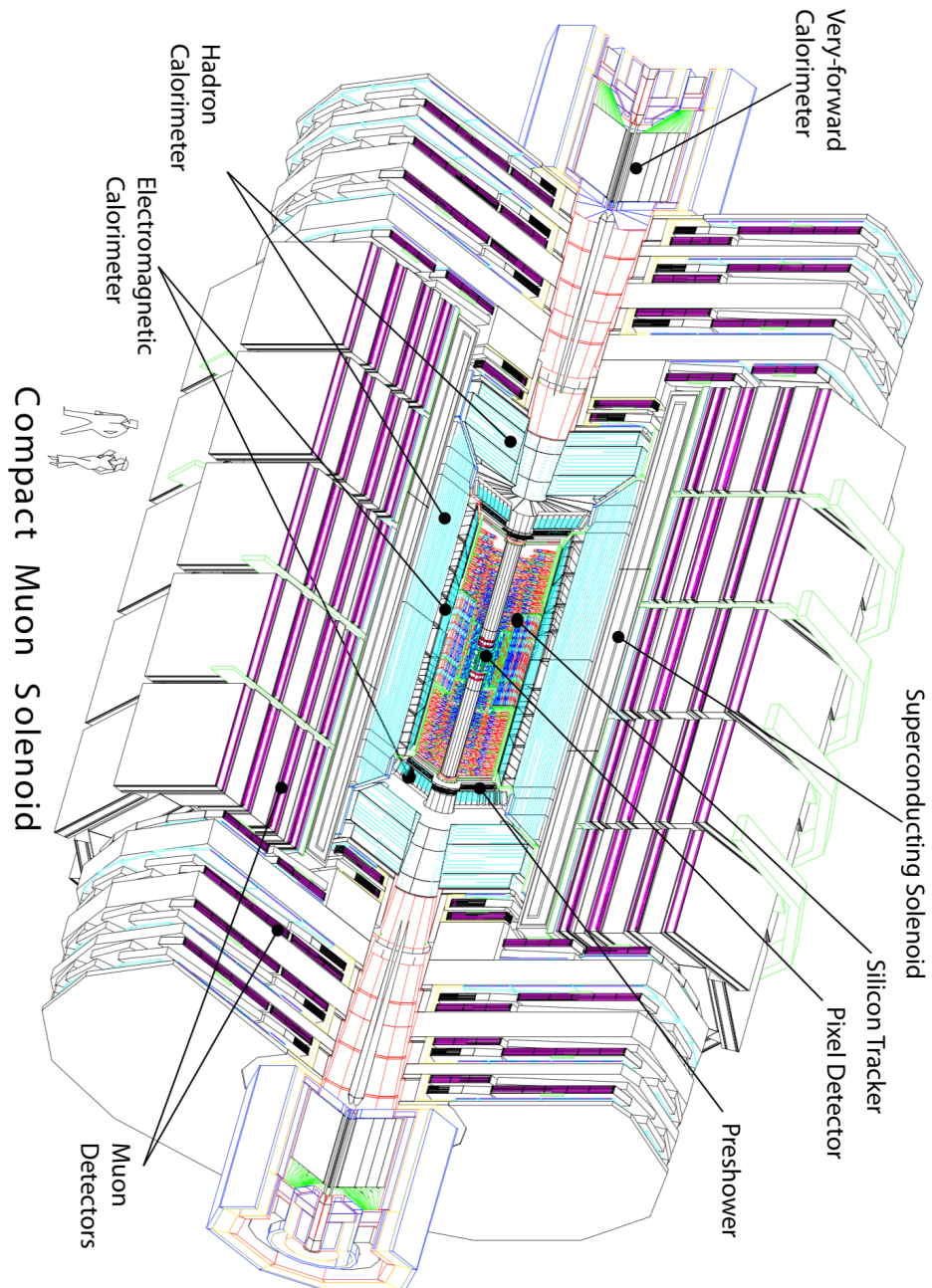


Figure 2.1.: Cross-section view of CMS.

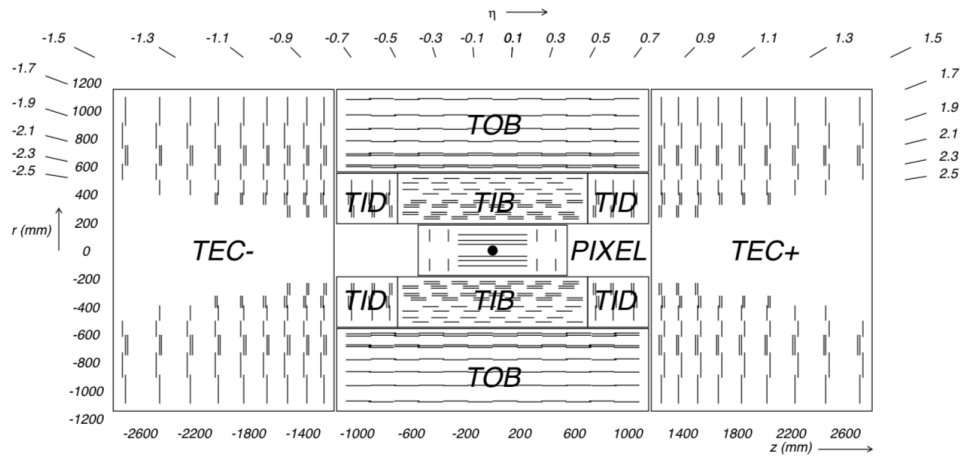


Figure 2.2.: Schematic cross-section through the CMS tracker, where a single detector modules is represented by a line, and double lines signify back-to-back modules.

Chapter 3.

Event Reconstruction

In order to target $t\bar{t} + \chi\bar{\chi}$ production in the dilepton final state, where both top quarks have leptonically decaying W bosons, the selection criteria is compatible with that of SM $t\bar{t}$ decays in the dilepton final state, but with an additional requirement that the event contain a moderate amount of p_T^{miss} .

Sections 3.1 are dedicated to the necessary criteria each object in an event must adhere to for consideration as a potential signal event.

3.1. Leptons

A top and anti-top quark are expected in the signal event, and each emits a W^+ and W^- respectively. The W^\pm boson in turn decays to a lepton and its corresponding lepton neutrino, as shown in Figure 3.1. Although the W^\pm boson decays democratically to each lepton generation, only the first and second generation are considered in this analysis. Namely, since the top and anti-top produce a positively and negatively charged W boson, the final state topology is expected to contain two oppositely

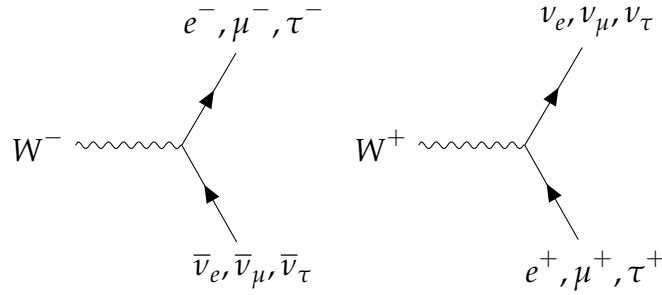


Figure 3.1.: W^+ and W^- decay to leptons and corresponding lepton neutrinos for all lepton generations.

charged leptons of either the same lepton flavor or opposite lepton flavor. The term flavor is used to distinguish between the first and second lepton generations. Thus, events with two electrons (ee), two muons ($\mu\mu$), or an electron and muon pair ($e\mu$) are selected. τ leptons are not considered because of challenges in detector reconstruction.

3.1.1. Muons

In order to be selected, muons must pass a stringent set of criteria which guarantee a high muon identification efficiency. The following list of criteria describe the “Tight” working point employed to select a well-identified muon:

- *Global Muon* (outside-in) reconstruction: A standalone muon in the outer muon detectors is matched to a tracker track and a *global-muon track* is fitted, which combines hits from the tracker track and standalone-muon track.
- *Tracker Muon* (inside-out) reconstruction: Tracker tracks with $p_T > 0.5 \text{ GeV}/c$ and $p > 2.5 \text{ GeV}/c$ are taken to be muon candidates and are extrapolated to the muon system, factoring in energy loss expected and the uncertainty from multiple scattering. An extrapolated track qualifies as a tracker-muon track if it is matched with at least one short stub from DT or CSC hits.

- *Particle Flow Muon* identification: As a general definition, the Particle Flow (PF) algorithm combines information from all CMS subdetectors in order to reconstruct and identify individual particles. For muons, the PF algorithm applies selection criteria on the reconstructed *Global Muon* and *Tracker Muon* dependent on the environment of the muon. The criteria are modified accordingly to the environment, in order to make use of the pertinent sub-detectors. For example, energy deposits in the calorimeter may be used to assign the momentum of a muon that is not well isolated.
- $\chi^2/\text{ndof} < 10$ for *Global Muon* track fit: intended to suppress particles originating from hadronic punchthrough
- At least one muon-chamber hit included in *Global Muon* track fit: This requirement is intended to suppress particles originating from hadronic punchthrough and muons coming from in-flight decays
- Muon segments in at least two muon stations: A tracker track must be matched to these segments, using more than 10 inner-tracker hits, with at least 5 tracker layers containing hits, and at least one pixel hit. This suppresses the punchthrough rate, any accidental track-to-segment matching, and guarantees a good p_T measurement.
- $|d_{xy}| < 2$ mm: The tracker track must have a transverse impact parameter, d_{xy} , less than 2 mm with respect to the location of the primary vertex interaction point. This requirement is intended to suppress backgrounds from cosmic muons and further suppress muons originating from in-flight decays.
- $|d_z| < 5$ mm: The tracker track must have a longitudinal distance, d_z , less than 5 mm with respect to the location of the primary interaction vertex in order to

further suppress cosmic muons, muons originating from in-flight decays, and tracks from pile-up.

In addition to the aforementioned selection criteria, to further reduce contamination from jets, muon candidates are required to be isolated from all other reconstructed particles within a radius of 0.4 according to the isolation variable defined as,

$$I = I_{h^+} + \max \left(I_{h^0} + I_{\gamma} - 0.5 \cdot I_{\text{pu}}, 0 \right). \quad (3.1)$$

where h^+ , γ , and h^0 correspond to charged hadrons, photons, and neutral hadrons, respectively, and each I quantity is the sum p_T (sum E_T for γ , and h^0) of these particle types in the $R = 0.4$ cone. I_{pu} is the contribution from charged hadrons from pileup and is referred to as the $\Delta\beta$ correction meant to account for effects of additional charged particles not associated with the primary vertex. The value computed in Eq. 3.1 is divided by the muon p_T which is not included in the calculation, hence the value is turned into a relative isolation, I_{rel} . Muons in the event are required to have a relative isolation of less than 0.15.

A looser set of muon identification and isolation requirements are also used in this analysis. In one case the “Fake-able Object” (FO) working point is employed in a background estimation method described later. In addition, a “Loose” muon identification and isolation working point is also used to veto any additional muons in an event. The three muon working points are summarized in Tab. 3.1.

Variable	FO WP	Loose WP	Tight WP
PF-muon	true	true	true
global muon	-	-	true
global OR tracker muon	true	true	-
χ^2/ndof of global muon fit <	-	-	10
No. of muon chamber hit in global muon fit \geq	-	-	1
No. of muon stations with muon segments \geq	-	-	2
$ d_{xy} $ (cm) <	-	-	0.2
$ d_z $ (cm) <	-	-	0.5
No. of pixel hits >	-	-	0
No. of tracker layers with hits >	-	-	5
relative isolation <	0.4	0.25	0.15
track isolation <	0.4	-	-

Table 3.1.: Variables and thresholds that define “FO”, “Loose”, and “Tight”. “-” indicates the variable is not considered for that working point.

3.1.2. Electrons

Electrons must also pass a stringent set of selection requirements in order to be considered a candidate component of the signal event. The criteria are outlined in the following list:

- $\sigma_{i\eta i\eta}$: This variable describes the lateral extension of the hadronic shower along the η direction. It is defined as,

$$(\sigma_{i\eta i\eta})^2 = [\sum (\eta_i - \bar{\eta})w_i] / \sum w_i \quad (3.2)$$

and the sum runs over the 5x5 matrix of crystals around the highest E_T crystal of the supercluster (SC), and w_i denotes a weight that is logarithmically dependent on the contained energy.

- $|\Delta\phi_{in}| = |\phi_{SC} - \phi_{in}^{\text{extrap}}|$: This denotes the azimuthal separation between the SC energy-weighted ϕ position and the track ϕ extrapolated from the innermost track position and direction to the point of closest approach (PCA) to the SC.
- $|\Delta\eta_{in}| = |\eta_{SC} - \eta_{in}^{\text{extrap}}|$: This denotes the lateral separation between the SC energy-weighted η position and the track η position extrapolated from the innermost track position and direction to the PCA to the SC.
- H/E : The ratio between the energy deposits in the HCAL and ECAL supercluster.
- $|1/E - 1/p|$: This quantity expresses an energy-momentum matching requirement using the SC energy, E , and the track momentum, p , at the PCA to the track vertex. The requirement helps to reject backgrounds from hadronic activity where the spread of the E is not localized resulting in a low E/p , but also backgrounds where a π^0 decays to e^+e^- in the close vicinity of a charged hadron, resulting in a very high E/p ratio.
- $|d_{xy}|$: The transverse impact parameter of the tracker track with respect to the primary interaction vertex.
- $|d_z|$: The longitudinal impact parameter of the tracker track with respect to the primary interaction vertex.
- Missing hits: After track-fitting is performed to electron-tracks seeded by an ECAL crystal with maximum energy in a considered region, if several tracker hits are found to be compatible with those expected in a layer from the track trajectory, at most one missing hit is allowed for an accepted candidate. Furthermore, in order to avoid the inclusion of hits originating from bremsstrahlung photons converted to e^+e^- pairs, in the reconstruction of primary electron tracks, an increased χ^2 penalty is applied to trajectory candidates which have one missing hit.

- Pass conversion veto: In order to reject secondary electrons produced in the conversion of photons in the tracker material, a vertexing algorithm is used. The hits in the tracker from the converted photon are fit to a common vertex using the well-defined topological constraint that tracks from conversions have virtually the same tangent at the conversion vertex in both the (r, ϕ) and (r, z) planes. The converted photon candidates are rejected according to the χ^2 probability of the fit.

In addition to the aforementioned selection criteria, electrons are required to be isolated from nearby activity, namely significant energy flow that may be a result of misidentified jets or that may be due to genuine electrons within a jet resulting from a semileptonic b or c quark decay. Similarly to the isolation definition for muons in Eq. 3.1, the electron isolation definition is a sum of PF-candidates within $R = 0.3$ of the electron. Explicitly, the isolation is computed as,

$$I = I_{h^+} + \max \left(I_{h^0} + I_{\gamma} - A_{eff} \cdot \rho, 0 \right), \quad (3.3)$$

where I_{h^+} , I_{h^0} , and I_{γ} are the contributions from charged hadrons, neutral hadrons, photons, respectively. ρ denotes the event energy density. Effects due to pileup are mitigated using corrections based on the “effective area”, denoted as A_{eff} in Eq. 3.3. In order to obtain the A_{eff} , the isolation is plotted as a function of ρ in bins of η , and the value at which the isolation is 90% efficient is determined in slices of ρ , known as the cutoff. A first order polynomial is fit to the cutoff and the slope is taken as the value of the correction, as listed in Tab. 3.2 for the various $|\eta|$ ranges.

A looser set of electron identification and isolation requirements are also used in this analysis. In one case the “Fake-able Object” (FO) working point is employed in a background estimation method described later. In addition, a “Veto” electron identi-

$ \eta $ range	A_{eff}
0.0 – 1.0	0.1703
1.0 – 1.479	0.1715
1.479 – 2.0	0.1213
2.0 – 2.2	0.1230
2.2 – 2.3	0.1635
2.3 – 2.4	0.1937
2.4 – 2.5	0.2393

Table 3.2.: Effective areas for electron isolation PU subtraction.

fication and isolation working point is also used to veto events with any additional electrons. The three electron working points are summarized in Tab. 3.3, for both the barrel and endcap regions, where an electron is defined as being in the barrel if it has a supercluster $|\eta| < 1.479$.

Variable	FO WP		Veto WP		Tight WP	
	Barrel	Endcap	Barrel	Endcap	Barrel	Endcap
$\sigma_{i\eta i\eta} <$	0.011	0.031	0.0115	0.037	0.00998	0.0292
$\Delta\eta_{in} <$	0.04	-	0.00749	0.00895	0.00308	0.00605
$\Delta\phi_{in} <$	0.02	-	0.228	0.213	0.0816	0.0394
H/E	0.06	0.06	0.356	0.211	0.0414	0.0641
$ 1/E - 1/p <$	0.013	0.013	0.299	0.15	0.0129	0.0129
$ d_{xy} \text{ (cm)} <$	0.1	0.2	0.05	0.10	0.05	0.10
$ d_z \text{ (cm)} <$	0.373	0.602	0.10	0.20	0.10	0.20
No. of missing expected hits \leq	1	1	2	3	1	1
relative isolation $<$	-	-	0.175	0.159	0.0588	0.0571
relative ECAL PFCluster iso $<$	0.16	0.12	-	-	-	-
relative HCAL PFCluster iso $<$	0.12	0.12	-	-	-	-
relative track iso $<$	0.08	0.08	-	-	-	-
pass conversion veto	true	true	true	true	true	true

Table 3.3.: Variables and thresholds that define “FO”, “Veto”, and “Tight” electrons. An electron is in the barrel if it has supercluster $|\eta| < 1.479$, otherwise it is in the endcap.

3.2. Jets

Jets are reconstructed from particle candidates obtained by the PF algorithm, using the anti- k_T clustering algorithm with size parameter, $R = 0.4$.

The anti- k_T algorithm is part of a group of sequential jet clustering algorithms that make use of the distance between candidate particles and their respective energies when forming a jet. Such algorithms make the assumption that the particles contained in a jet have minimal differences in p_T , hence the grouping is performed based on momentum-space. These algorithms share a similar underlying method where a distance is computed between two candidate particles according to:

$$d_{ij} = \min \left(p_{T_i}^a, p_{T_j}^a \right) \times \frac{R_{ij}^2}{R} \quad (3.4)$$

where $R_{ij} = (\eta_i - \eta_j)^2 + (\phi_i - \phi_j)^2$ is the $(\eta - \phi)$ distance between the two particles and R is the radius parameter of the jet cone. These methods also require the computation of a second distance variable, $d_{iB} = p_{T_i}^a$, the momentum-space distance between the beam axis and the candidate particle. Subsequently, the minimum of the entire set d_{ij}, d_{iB} is determined and if d_{ij} is the minimum, then particles i and j are combined by the summation of their respective four-vectors, and removed from the list of particles. If d_{iB} is determined as the minimum, the candidate i is taken as the final jet and removed from the list of particles. The process is repeated until either a desired number of jets have been found (exclusive), or the separation between particles in a jet, R_{ij} , is greater than the jet size parameter R (inclusive).

In the anti- k_T algorithm, the value of a corresponds to -2, such that Eq. 3.4 results in,

$$d_{ij} = \min \left(\frac{1}{p_{Ti}^2}, \frac{1}{p_{Tj}^2} \right) \times \frac{R_{ij}^2}{R} \quad (3.5)$$

and $d_{iB} = \frac{1}{p_{Ti}^2}$. The anti- k_T algorithm is minimally affected by activity from the underlying event and pile-up, since Eq. 3.5 is dominated by high p_T particles, so the algorithm preferentially begins clustering hard particles, causing the jet area to fluctuate a small amount.

In order to reduce the effects of “in-time” pile-up, that is additional pp collisions occurring in the same bunch-crossing as the collision of interests, a charge hadron subtraction (CHS) treatment is performed during the anti- k_T clustering of PF jets. The CHS technique removes any charged hadrons well-matched to PU vertices, allowing for the clustering of remaining PF candidates to form jets. In the PF algorithm, a charged hadron is defined as a track possibly associated with hits in the ECAL and HCAL. In order to determine a primary vertex, the proto-vertex with the largest magnitude of the sum of squares of the track transverse momenta $\left(\sum |p_T^{TRK}|^2 \right)$ is chosen. Subleading vertices are deemed as originating from PU and their minimum degrees of freedom, N_{dof} , in the vertex fit is required to be larger than four. Based on the chi-square per degree of freedom ($\chi^2/\text{d.o.f}$), a charged hadron can be assigned to the chosen PV if this value is less than 20, otherwise it is associated to a PU vertex. The final step of the CHS procedure entails the removal of PU tracks which are determined by the association of the charged hadron track to a good PU PV. The tracks associated to the PV, and any other tracks not associated to the PU vertices, are kept. The primary effect of the application of CHS is the removal of jets from pileup, although the procedure also improves the angular and p_T resolution of jets, along with reducing the rate of low p_T jets created solely from PU in the tracker acceptance region ($|\eta| < 2.5$).

Furthermore, a set of loose identification criteria on the relative fractions of reconstructed PF jet constituents are imposed in order to suppress noise contributions from the HCAL and ECAL. The PF candidates are denoted as “charged EM” (electron or muon), “neutral EM” (photon), “charged hadron”, and “neutral hadron”, and the requirements are made on the relative jet energy fraction that are carried by each type. Tracker acceptance limits the validity region of the “charged” variables to $|\eta| < 2.4$, however the “neutral” variables extend up to $|\eta| < 5$. The “loose” PF jet identification working point defined in Tab. 3.4 targets the removal of jets emerging from calorimetric noise.

Variable	$ \eta < 2.7$	$2.7 < \eta < 3$	$ \eta > 3$
Neutral Hadron Fraction	< 0.99	< 0.98	-
Neutral EM Fraction	< 0.99	> 0.01	< 0.9
Number of Constituents	> 1	-	-
Number of Neutrals	-	> 2	> 10
<i>Additional cuts for $\eta < 2.4$</i>			
Charged Hadron Fraction	> 0		
Charged Multiplicity	> 0		
Charged EM Fraction	< 0.99		

Table 3.4.: Variables and thresholds that define the “Loose” PF jet ID.

The jet is not considered if it is within $\Delta R < 0.4$ of a “Tight” electron or muon.

3.2.1. b jet tagging

In addition to the preceding jet requirements, an algorithm developed to distinguish jets originating from the hadronization of b quarks is employed in the analysis. This identification relies heavily on the precise reconstruction of secondary vertices associ-

ated to weakly decaying b hadrons present in jets origination from the hadronization of b quarks.

The algorithm, known as the Combined Secondary Vertex (v2) (CSV) makes use of the Inclusive Vertex Finder (IVF), which is exploited in the reconstruction of secondary vertices. The IVF is seeded by a collection of reconstructed tracks in the event which satisfy a loose set of requirements, such that tracks with at least 8 hits in the silicon pixel tracker are selected. The selected tracks must have a p_T greater than 0.8 GeV and the longitudinal impact parameter, the distance between the primary vertex and the track at their point of closest approach, should be smaller than 0.3 cm. In order to create the secondary vertices, the tracks must be displaced, having an IP no larger than $50 \mu m$ and IP significance (IP divided by its uncertainty) of at least 1.2. Clusters are then formed from the displaced seed tracks using requirements on minimum distances and the opening angles between them. An adaptive vertex fitter is used to fit the clusters. The vertex reconstruction algorithm then proceeds with multiple iterations of track arbitration in order to appropriately associate the cluster tracks with the primary or secondary vertex. Each step makes requirements on the fraction of tracks from the secondary vertex shared with the primary and the angular distances between the two vertices.

The CSV algorithm subsequently makes use of the tracks and vertices passing the requirements of the IVF. In the CSV algorithm, at least two displaced tracks identified with the IVF procedure are required within a jet, and furthermore must have an angular distance, ΔR , less than 0.3 with respect to the jet axis. The CSV algorithm categorizes the input vertices into three independent categories. The categories are listed and briefly defined below.

- Jets are associated with at least one reconstructed SV: Vertices are sorted according to increasing uncertainty on the flight distance if more than one reconstructed SV

is found. Most discriminating variables relying on a SV are such that the leading SV is required, such as the vertex mass or the flight distance significance.

- Jets are associated with a “pseudo-vertex”: No vertex fit is applied to candidates satisfying this category since the jet contains at least two tracks incompatible with a window of 50 MeV around the K_s^0 meson mass and a signed IP larger than 2. Since the calculation of a flight distance is not feasible, the discriminating variables are reduced in this category as compared to the previous.
- Jets are not associated with any reconstructed SV or “pseudo-vertex”: This category compliments the above two, meaning only variables related to the displaced track vertex are exploited.

The variables defined in each category are combined in each respective category via a multilayer perceptron (MLP) with one hidden layer. An MLP is a type of artificial neural network where the information in each layer is fed uni-directionally to the next. It has the advantage of distinguishing non-linearly separable data. A likelihood ratio taking into account the expected fraction of jet flavors in $t\bar{t}$ events is combined with the information from the three categories, to yield the final CSV discriminant, as shown in Figure 3.2, for multi-jet events where at least one jet satisfies an online p_T requirement of greater than 40 GeV.

3.3. Missing transverse energy

A crucial aspect of this search requires the precise modeling of the missing transverse momentum, denoted \vec{p}_T^{miss} , and its magnitude, referred to as the missing transverse energy, and denoted by p_T^{miss} . Owing to momentum conservation, \vec{p}_T^{miss} corresponds to the transverse momentum that is carried by weakly interacting particles, such

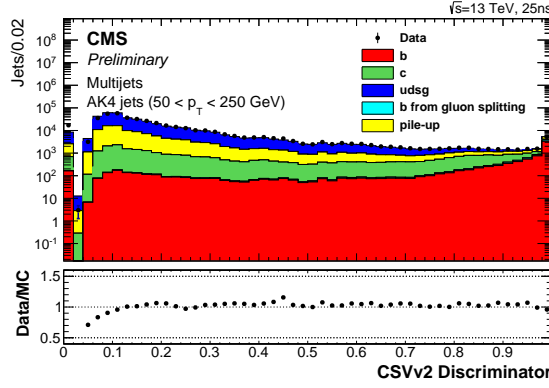


Figure 3.2.: Discriminator values for the CSVv2 algorithm for an inclusive multi-jet topology, where the total number of entries in the simulation is normalized to the observed number of entries in the data.

as neutrinos. This observable is of particular importance in the search for $t\bar{t} + \chi\bar{\chi}$, since the neutral DM particles are also predicted to interact weakly, hence they will escape the detector volume without being detected. Consequently, the measurement of p_T^{miss} relies heavily on the detectable and reconstructed physics objects mentioned in the preceding sections. Thus, p_T^{miss} is defined as the imbalance in the transverse momentum of all particles that interact with the detectors. As mentioned in Sec. , the CMS PF algorithm reconstruction uses all the available detector information to create a list of identified and reconstructed PF particles. It then follows that the \vec{p}_T^{miss} is defined as the negative vectorial sum of the transverse momenta of all PF particles reconstructed in the event, such that,

$$\vec{p}_T^{\text{miss}} = - \sum_{i=\text{PF particles}} \vec{p}_{Ti} \quad (3.6)$$

The measurement of the p_T^{miss} can be mismeasured as a cause of a variety of reasons. The nonlinear response of the calorimeter for neutral and charged hadrons due to its noncompensating nature, minimum energy thresholds in the calorimeters,

inefficiencies in the tracker, or neutrinos from semileptonic particle decays are a sources from which bias can be introduced in the p_T^{miss} measurement. In order to mitigate these biases, the p_T^{miss} derived from PF particles, denoted by $\text{PF-}p_T^{\text{miss}}$, is corrected for using jet energy scale corrections, so Eq. 3.6 then becomes,

$$\text{PF}\vec{p}_T^{\text{miss}} = \text{PF}\vec{p}_T^{\text{miss}} - \sum_{\text{jets}} \left(\vec{p}_{T,\text{jet}}^{\text{corr}} - \vec{p}_{T,\text{jet}} \right) \quad (3.7)$$

All jets with $p_T > 15 \text{ GeV}$ and less than 0.9 of their energy deposited in the ECAL are corrected. In addition, the muon four-momentum is subtracted from the jet four-momentum when the correction is performed, if a muon is found within a jet. Jet energy corrections consist of several stages and are derived and applied in a factorized manner, although the underlying procedure of scaling the jet four-momentum with a scale factor (SF) which depends on jet quantities such as p_T , η , and flavor is universal. The corrections are listed and described briefly below in the order they are applied.

- L1 Pile up: Aimed at removing any energy contributions from pile-up events, this correction is determined from a simulation sample of QCD dijet events which are processed with and without pileup overlay. The corrections are parametrized as a function of the jet area (A), jet η and p_T , and the offset energy density (ρ). The correction applied to data is parametrized in η and determined using zero bias events.
- L2L3 MC-truth corrections: The reconstructed jet p_T is compared to the particle level jet p_T in order to derive jet response corrections from a QCD dijet simulation sample. The jet response is made uniform over p_T and η , the jet variables in which it is derived.

- L2L3 Residuals: These corrections are applied to jets in data and include both an η and p_T component. For the η dependence (relative corrections), dijet events are compared to a jet of similar p_T in the barrel region ($|\eta| < 1.3$). For the p_T dependence (absolute corrections), the JES relative to the reference JES of the barrel jet is taken into account. The jet absolute scale corrections are derived using $Z(\mu\mu/ee)+\text{jets}$, photon+jet, and multijet events.

3.4. Event Selection

The objects defined in Sec. 3.1-3.3 are all employed to target the selection of events consistent with $t\bar{t} + p_T^{\text{miss}}$ where both tops have leptonically decaying W bosons. The selection for the signal region is the following,

- Two “Tight” leptons with opposite charge (ee or $e\mu$ or $\mu\mu$) with $p_T > 25$ GeV for the leading lepton and $p_T > 15$ GeV for the trailing lepton,
- No additional leptons with $p_T > 10$ GeV and passing “Loose” muon or “Veto” electron criteria,
- Two or more jets where at least one jet is b-tagged,
- $M_{\ell\ell} > 20$ GeV,
- $|M_{\ell\ell} - M_Z| > 15$ GeV for ee and $\mu\mu$ events,
- $p_T^{\text{miss}} > 50$ GeV,

Dilepton candidate events with an invariant mass $M_{\ell\ell} < 20$ GeV are removed in order to suppress any backgrounds from low-mass Drell-Yan processes, as well as any contributions from heavy-flavor resonances. The requirement for events in the same flavor (ee and $\mu\mu$) channel to have an invariant mass ± 15 GeV away from the Z boson

pole mass is also used to reject $Z(\ell\ell)$ background events. The moderate requirement of $p_T^{\text{miss}} > 50 \text{ GeV}$ aims to further suppress contamination from DY events in the same flavor channel.

3.4.1. The $M_{T2}^{\ell\ell}$ variable

Along with categorization according to lepton flavor (same or opposite), events are also categorized based on the stransverse mass quantity, $M_{T2}^{\ell\ell}$, defined as,

$$M_{T2}^{\ell\ell} = \min_{\vec{p}_{T1}^{\text{miss}} + \vec{p}_{T2}^{\text{miss}} = \vec{p}_T^{\text{miss}}} \left(\max \left[M_T \left(\vec{p}_T^{\ell_1}, \vec{p}_{T1}^{\text{miss}} \right), M_T \left(\vec{p}_T^{\ell_2}, \vec{p}_{T2}^{\text{miss}} \right) \right] \right), \quad (3.8)$$

$M_{T2}^{\ell\ell}$ is partially motivated from the transverse mass, denoted $M_T \left(\vec{p}_T^\ell, \vec{p}_T^{\text{miss}} \right)$ in Eq. 3.8, where the most notable use of M_T is in the measurement of the W boson mass in the $W \rightarrow \ell\nu$ decay mode. The transverse mass, defined in the context of a leptonic W boson decay, is as follows,

$$M_T = \sqrt{M_\ell^2 + M_\nu^2 + 2(E_T^\ell E_T^\nu - \vec{p}_T^\ell \cdot \vec{p}_T^\nu)} \quad (3.9)$$

where M_ℓ and M_ν are the masses of the lepton and neutrino, respectively, and \vec{p}_T^ℓ and \vec{p}_T^ν are their transverse momenta. E_T^ℓ and E_T^ν denote their transverse energies.

The utility of M_T is best for cases wherein one missing particle is expected (i.e. the neutrino in the leptonic W decay). However, once more than one missing particle is expected in an event, it is no longer possible to calculate the M_T since the p_T of an

individual missing particle cannot be resolved. Recalling that $t\bar{t} + \chi\bar{\chi}$ production and decay follows this route:

$$pp \rightarrow t\bar{t} + \phi \rightarrow W^+b + W^-\bar{b} + \chi\bar{\chi} \rightarrow \ell^+\nu b + \ell^-\bar{\nu}\bar{b} + \chi\bar{\chi}, \quad (3.10)$$

a signal event is expected to contain four particles that leave their signature in the detector collectively as p_T^{miss} , namely the ν , $\bar{\nu}$, χ , $\bar{\chi}$. Similarly, in the case of the SM $t\bar{t}(2\ell)$ process, the two lepton neutrinos are the sole contributors to the total \vec{p}_T^{miss} , and as postulated by the authors in [6], if the \vec{p}_T^{ν} and $\vec{p}_T^{\bar{\nu}}$ were obtainable, the maximum M_T value is bounded from above by the W boson mass such that,

$$M_W^2 \geq \max \left\{ M_T^2 \left(\vec{p}_T^{\ell^+}, \vec{p}_T^{\nu} \right), M_T^2 \left(\vec{p}_T^{\ell^-}, \vec{p}_T^{\bar{\nu}} \right) \right\}. \quad (3.11)$$

The partitioning of the \vec{p}_T^{miss} is however unknown, since neither the energy nor direction of either neutrino four-vector can be resolved, so the best that can be assumed is,

$$M_W \geq M_{T2}^{\ell\ell} = \min_{\vec{p}_{T1}^{\text{miss}} + \vec{p}_{T2}^{\text{miss}} = \vec{p}_T^{\text{miss}}} \left(\max \left\{ M_T \left(\vec{p}_{T1}^{\ell_1}, \vec{p}_{T1}^{\text{miss}} \right), M_T \left(\vec{p}_{T2}^{\ell_2}, \vec{p}_{T2}^{\text{miss}} \right) \right\} \right). \quad (3.12)$$

The minimization in Eq. 3.12 occurs over all the possible two-way partitions of \vec{p}_T^{miss} in the event. For the case of the SM $t\bar{t}(2\ell)$ background, a kinematic endpoint in the $M_{T2}^{\ell\ell}$ distribution, shown in Figure 3.3, occurs at the W boson pole mass. With this in mind, two signal regions are formed using the $M_{T2}^{\ell\ell}$ variable, where events with $M_{T2}^{\ell\ell}$

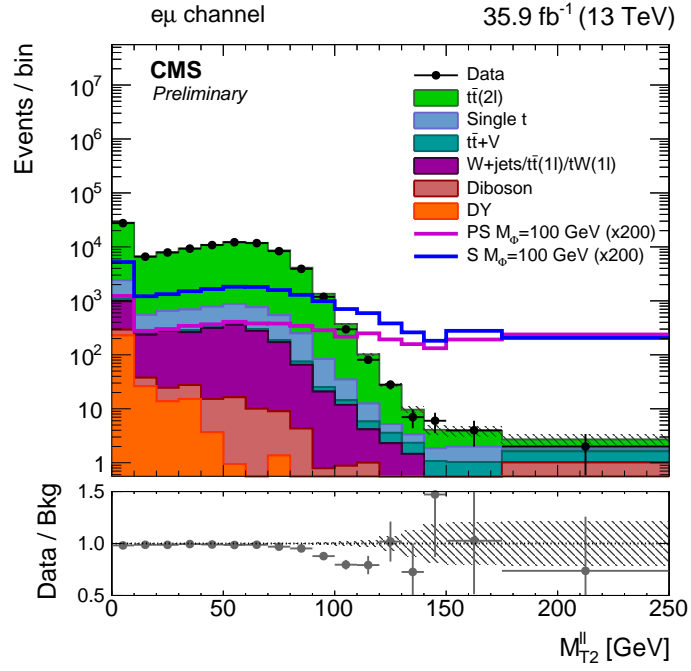


Figure 3.3.: The $M_{T2}^{\ell\ell}$ distribution in data and simulation for events passing selection requirements for the $e\mu$ channel. The distribution of two example signals (scalar and pseudoscalar mediator, $m_{\phi/a} = 100$ GeV) with $m_\chi = 1$ GeV is scaled up by a factor of 200. The last bin includes overflow. Uncertainties are statistical only.

> 110 GeV comprise the high signal purity region, since the signal is not expected to be contained in the region below the M_W as is the case for the SM $t\bar{t}(2\ell)$ background. The low signal purity category is formed by the remaining events, for which $M_{T2}^{\ell\ell} < 110$ GeV.

Chapter 4.

Background processes

Two classes of background processes are present in this search: reducible and irreducible. For the former category, a particle in the background process may “fake” the signature of a particle that is expected in the signal process. On the contrary, in the case of the latter category, the final state topology of the background process yields the same expected particles as a potential signal process. A key feature of reducible backgrounds is the ability to suppress such processes by employing the selection cuts as described in Sec. 3.4. Furthermore, some of the reducible background contributions are estimated using data-driven techniques. In large part, however, the dominant backgrounds in the search are estimated from simulations.

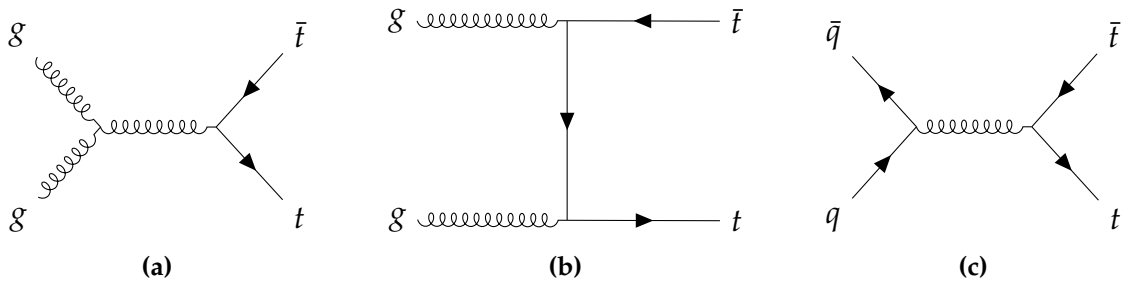


Figure 4.1.: Leading order $t\bar{t}$ production diagrams probed at the LHC via (a), (b) gluon fusion, and (c) quark-antiquark annihilation.

4.1. $t\bar{t}(2\ell)$

SM $t\bar{t}(2\ell)$ is the dominant background contribution and is irreducible, owing to the similarity of the final state topology with the signal processes topology. At the LHC, approximately 90% of $t\bar{t}$ events are produced via gluon fusion as shown in Figure 4.1a and Figure 4.1b, in contrast to the Tevatron at Fermilab, where quark-antiquark annihilation shown in Figure 4.1c constituted roughly 85-90% of the relative $t\bar{t}$ production.

The theoretical uncertainties incurred at leading order (LO) in perturbative QCD are quite large for $t\bar{t}$ production. In addition to the LO simulation, the $t\bar{t}$ process decaying to the dilepton final state is simulated at next-to-leading order (NLO) using the POWHEG (v2) [7, 8] generator, with the top quark mass assumed to be $m_{\text{top}} = 172.5$ GeV. These events are then interfaced to Pythia (v8.2) [9] for parton fragmentation, hadronization, and to simulate the underlying event. As pertains to all simulated samples subsequently described, once the $t\bar{t}(2\ell)$ events are showered, the detector response is simulated using the GEANT4 program [10]. Finally, the $t\bar{t}(2\ell)$ events are normalized to the theoretical cross section calculated at next-to-next-to-leading order (NNLO) in perturbative QCD, which also includes soft-gluon resummation calculations at next-to-next-to-leading-order (NNLL) [11–15]. The cross-section folds in the branching fraction of $t\bar{t}$ to the dilepton final state, which is 10.5%. The cross-section value used is $\sigma_{t\bar{t}(2\ell)} = 87.31$ pb.

As mentioned in Sec. 3.4.1, the $t\bar{t}(2\ell)$ background should be suppressed below the kinematic endpoint, M_W , in the $M_{T2}^{\ell\ell}$ distribution. This would only be possible in ideal measurement conditions, however as a cause of detector and energy resolution effects, the mismeasurement of the objects in $t\bar{t}(2\ell)$ background events can contribute to values of $M_{T2}^{\ell\ell} > M_W$.

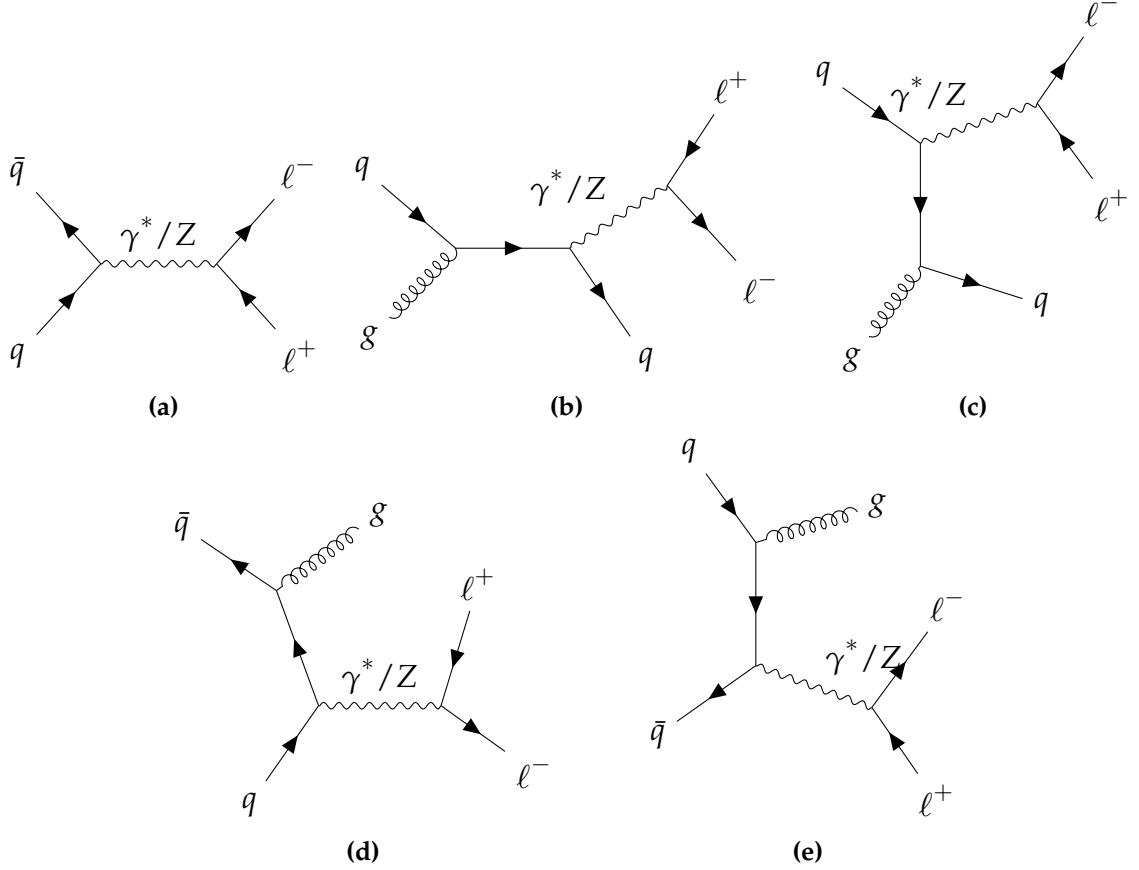


Figure 4.2.: The Drell-Yan lepton pair-production process mediated by a virtual photon (γ^*) or Z boson at (a) $\mathcal{O}(\alpha)$ and (b),(c),(d),(e) $\mathcal{O}(\alpha\alpha_s)$.

4.2. Drell-Yan

From the diagrams in Figure 4.2, the Drell-Yan pair-production process falls under the class of reducible backgrounds, since many of the selection criteria act to suppress processes where the selected same flavor opposite sign (SFOS) leptons are produced at the same vertex, such as from the exchange of a real Z boson or a virtual photon (γ^*). Namely, the requirement for the mass of the selected SFOS lepton pair to be outside of the Z mass window, $75 \text{ GeV} < M_Z < 105 \text{ GeV}$, removes a large contribution of dilepton decays stemming from real Z bosons/off-shell virtual photons. Furthermore, the low dilepton mass requirement, $M_{\ell\ell} > 20 \text{ GeV}$ suppresses the contribution from low mass

decays of J/ψ mesons to SFOS pairs. In addition, the requirement for the event to contain at least two jets, with at least one b-tagged jet acts to eliminate contributions from Figure 4.2a, where the quark-antiquark annihilation to a SFOS pair proceeds at LO in α . The DY process is simulated at NLO using the MADGRAPH5_AMC@NLO generator (v5.2.3.3) [16], and thus includes contributions from higher order processes as shown in Figure 4.2b-Figure 4.2e, where at least one jet is expected from the fragmentation and hadronization of particles emitted in initial state radiation.

Although the relative shape of the DY contribution is taken from simulation, a data-driven process is used to estimate the normalization of this background. The signal region still contains a sizeable DY contribution, meaning that exceptional DY events evading the above-mentioned Z boson mass veto tend to be accompanied by a significant amount of p_T^{miss} . Since the instrumental detector effects which influence this final state topology are non-trivial to simulate, it is more appropriate to use calibrated samples from data to arrive at these estimates.

4.2.1. The $R_{\text{in/out}}$ method

The method is used to predict the DY normalization, N_{DY} , by extrapolating from the observed DY yield inside the Z mass window (within $\pm 15 \text{ GeV}$ of M_Z), N_{in} , according to:

$$N_{DY} = N_{in} \frac{R_{MC}^{0b}}{R_{MC}^{1b} \cdot R_{\text{data}}^{0b}}, \quad (4.1)$$

where each quantity R in Eq. 4.1 is defined as the ratio of DY yields **inside** to **outside** the Z mass window,

$$R_{\text{in/out}} = \frac{N(|M_{\ell\ell} - M_Z| < 15 \text{ GeV})}{N(|M_{\ell\ell} - M_Z| > 15 \text{ GeV and } M_{\ell\ell} > 20 \text{ GeV})}. \quad (4.2)$$

Hence, the events originally rejected by the Z veto are used to estimate the residual contributions from $DY \rightarrow e^+e^-$ and $\mu^+\mu^-$ in the remaining selected sample. The yields are computed with all other selection cuts applied. Ideally, the $R_{\text{in/out}}$ in a region where the number of b-tagged jets is required to be zero would be equal to the $R_{\text{in/out}}$ in a region where at least one b-tagged jet is required, such that $R_{\text{in/out}}^{0b} = R_{\text{in/out}}^{1b}$. This assumption, however, is invalid since the numerator and denominator in Eq. 4.2 differ significantly when measured in DY simulation with a looser set of selection cuts, such as the removal of the p_T^{miss} requirement or a looser jet multiplicity requirement. A weaker assumption is then made, which is as follows:

$$\frac{(R_{\text{in/out}}^{1b})_{\text{data}}}{(R_{\text{in/out}}^{1b})_{\text{MC}}} = \frac{(R_{\text{in/out}}^{0b})_{\text{data}}}{(R_{\text{in/out}}^{0b})_{\text{MC}}}, \quad (4.3)$$

so the ratio of the measured $R_{\text{in/out}}^{0b}$ between data and MC should be equivalent to the ratio of the measured $R_{\text{in/out}}^{1b}$ between data and MC. Then the estimate for the DY normalization in the signal region as defined in Eq. 4.1 is expanded into,

$$(N_{\text{out}}^{1b})_{\text{data}} = \frac{(N_{\text{in}}^{1b})_{\text{data}}}{(R_{\text{in/out}}^{1b})_{\text{data}}} = \frac{(N_{\text{in}}^{1b})_{\text{data}}}{(R_{\text{in/out}}^{1b})_{\text{MC}}} \cdot \frac{(R_{\text{in/out}}^{0b})_{\text{MC}}}{(R_{\text{in/out}}^{0b})_{\text{data}}} \quad (4.4)$$

Thus, every quantity on the right-hand side of Eq. 4.4 is measured. However, it should be noted that non-DY contributions are present in the measurements made in the data, and hence must be subtracted off from events that fall both inside and outside the Z mass window in the zero b-tag and the one-or-more b-tag regions (i.e. all the quantities N_{in}^{0b} , N_{out}^{0b} , N_{in}^{1b} , and N_{out}^{1b}). The non-DY contributions in the $\{0b, 1b\} \otimes \{\text{in}, \text{out}\}$ regions, such as $t\bar{t}(2\ell)$, are estimated from data using opposite flavor (e^\pm, μ^\mp) events, that are denoted by $N_{\text{in}}^{e\mu}$ and $N_{\text{out}}^{e\mu}$. Thus, the number of events in data in each of the aforementioned regions, after the subtraction of non-DY backgrounds is,

$$N = N^{\ell\ell} - 0.5 \cdot k_{\ell\ell} \cdot N^{e\mu}, \quad (4.5)$$

where the 0.5 factor accounts for combinatorics, and $k_{\ell\ell}$ is a correction factor applied to account for the differences in reconstruction efficiencies between electrons and muons. The correction factor is derived from an inclusive selection targeting $Z \rightarrow \ell\ell$, and is defined as,

$$k_{ee} = \sqrt{\frac{N^{ee}}{N^{\mu\mu}}}, \quad k_{\mu\mu} = \sqrt{\frac{N^{\mu\mu}}{N^{ee}}} \quad (4.6)$$

The value for $k_{ee}(k_{\mu\mu})$ measured in data is 0.64 (1.55).

In order to capture any p_T^{miss} dependence of the DY normalization, the various $R_{\text{in/out}}$ quantities are computed in four bins of p_T^{miss} , shown in the fifth column of Table 4.1-Table 4.4, since the relative contribution of DY is expected to drop off at higher p_T^{miss} values and incur larger statistical uncertainties in the simulation. The “on” Z

peak (i.e. $|M_{\ell\ell} - M_Z| < 15 \text{ GeV}$) yields for a 0 b-tag selection listed in the second column of Table 4.1 and Table 4.2 can be seen in Figure 4.3 and Figure 4.4 for the ee and $\mu\mu$ channels, respectively. The predicted DY normalization in the signal region in each p_T^{miss} bin is listed in Table 4.5 and Table 4.6 under the column heading $(N_{\text{out}}^{1b})_{\text{data}}$. The simulation yields, under the column heading $(N_{\text{out}}^{1b})_{\text{MC}}$, are scaled by the factors in the last column of Table 4.5 and Table 4.6, and shown in Figure 4.5 in red and blue markers, respectively for the ee and $\mu\mu$ channel. The dashed line in Figure 4.5 represents the inclusively calculated scale factors, which are not used in the analysis but simply as a cross-check. The larger scale factors for the ee channel are attributed to a broader Drell-Yan line shape in data compared to simulation, while in the $\mu\mu$ channel the line shapes in data and simulation are more similar.

Table 4.1.: DY yields and $R_{\text{in/out}}$ values in the ee channel, for 0 b-tag selection

		$ M_{\ell\ell} - M_Z < 15 \text{ GeV}$	$ M_{\ell\ell} - M_Z > 15 \text{ GeV}$	$R_{\text{in/out}}^{0b}$
$50 \text{ GeV} < p_T^{\text{miss}} < 75 \text{ GeV}$	data	35602.72 ± 191.00	4912.88 ± 92.65	7.25 ± 0.14
	MC	38417.99 ± 233.36	4932.28 ± 155.12	7.79 ± 0.25
$75 \text{ GeV} < p_T^{\text{miss}} < 100 \text{ GeV}$	data	4503.12 ± 72.21	875.04 ± 61.05	5.15 ± 0.37
	MC	5651.58 ± 86.47	865.83 ± 58.83	6.53 ± 0.45
$100 \text{ GeV} < p_T^{\text{miss}} < 150 \text{ GeV}$	data	714.20 ± 37.79	415.24 ± 56.38	1.72 ± 0.25
	MC	746.41 ± 31.32	225.78 ± 21.53	3.31 ± 0.34
$150 \text{ GeV} < p_T^{\text{miss}} < 1000 \text{ GeV}$	data	221.68 ± 22.05	415.24 ± 56.38	0.53 ± 0.090
	MC	55.27 ± 7.33	105.28 ± 11.92	0.24 ± 0.040

Table 4.2.: DY yields and $R_{\text{in/out}}$ values in the $\mu\mu$ channel, for 0 b-tag selection

		$ M_{\ell\ell} - M_Z < 15 \text{ GeV}$	$ M_{\ell\ell} - M_Z > 15 \text{ GeV}$	$R_{\text{in/out}}^{0b}$
$50 \text{ GeV} < p_T^{\text{miss}} < 75 \text{ GeV}$	data	76878.78 ± 282.38	11061.48 ± 151.71	6.95 ± 0.099
	MC	84516.00 ± 353.40	12266.77 ± 277.25	6.89 ± 0.16
$75 \text{ GeV} < p_T^{\text{miss}} < 100 \text{ GeV}$	data	9757.90 ± 109.88	1551.43 ± 104.12	6.29 ± 0.43
	MC	11972.59 ± 130.57	2267.89 ± 104.23	5.28 ± 0.25
$100 \text{ GeV} < p_T^{\text{miss}} < 150 \text{ GeV}$	data	1468.25 ± 61.59	401.18 ± 96.96	3.66 ± 0.90
	MC	1639.18 ± 45.61	646.05 ± 43.72	2.54 ± 0.19
$150 \text{ GeV} < p_T^{\text{miss}} < 1000 \text{ GeV}$	data	305.85 ± 34.16	396.34 ± 97.66	0.77 ± 0.20
	MC	86.42 ± 10.45	290.42 ± 21.26	0.33 ± 0.018

Table 4.3.: DY yields and $R_{\text{in/out}}$ values in the ee channel, for ≥ 1 b-tag selection

		$ M_{\ell\ell} - M_Z < 15 \text{ GeV}$	$ M_{\ell\ell} - M_Z > 15 \text{ GeV}$	$R_{\text{in/out}}^{1b}$
$50 \text{ GeV} < p_T^{\text{miss}} < 75 \text{ GeV}$	data	5236.16 ± 90.60	—	—
	MC	5132.28 ± 84.32	623.60 ± 58.67	8.23 ± 0.79
$75 \text{ GeV} < p_T^{\text{miss}} < 100 \text{ GeV}$	data	1038.20 ± 58.76	—	—
	MC	915.35 ± 34.19	137.98 ± 22.97	6.63 ± 1.13
$100 \text{ GeV} < p_T^{\text{miss}} < 150 \text{ GeV}$	data	289.88 ± 51.08	—	—
	MC	193.95 ± 14.94	27.61 ± 8.35	7.02 ± 2.19
$150 \text{ GeV} < p_T^{\text{miss}} < 1000 \text{ GeV}$	data	154.72 ± 29.57	—	—
	MC	22.96 ± 5.00	17.32 ± 4.47	1.33 ± 0.45

Table 4.4.: DY yields and $R_{\text{in/out}}$ values in the $\mu\mu$ channel, for ≥ 1 b-tag selection

		$ M_{\ell\ell} - M_Z < 15 \text{ GeV}$	$ M_{\ell\ell} - M_Z > 15 \text{ GeV}$	$R_{\text{in/out}}^{1b}$
$50 \text{ GeV} < p_T^{\text{miss}} < 75 \text{ GeV}$	data	10398.33 ± 141.70	—	—
	MC	11001.22 ± 126.39	1444.20 ± 92.95	7.62 ± 0.50
$75 \text{ GeV} < p_T^{\text{miss}} < 100 \text{ GeV}$	data	1689.88 ± 97.73	—	—
	MC	1867.68 ± 50.40	293.68 ± 38.12	6.36 ± 0.84
$100 \text{ GeV} < p_T^{\text{miss}} < 150 \text{ GeV}$	data	372.47 ± 89.03	—	—
	MC	342.57 ± 21.09	113.32 ± 16.96	3.02 ± 0.49
$150 \text{ GeV} < p_T^{\text{miss}} < 1000 \text{ GeV}$	data	100.40 ± 49.44	—	—
	MC	30.05 ± 6.52	41.85 ± 9.82	0.72 ± 0.23

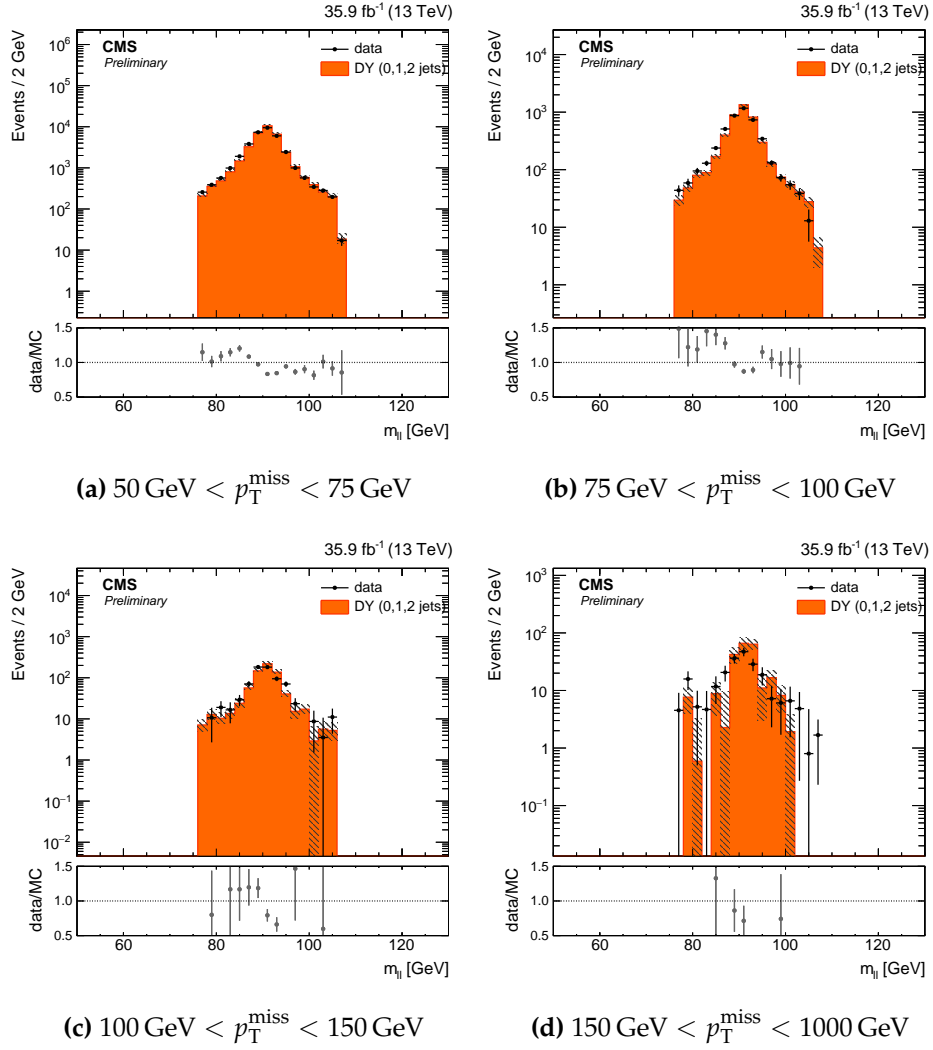


Figure 4.3.: Z peak in data and MC after subtraction of non-Drell-Yan contribution estimate from opposite-flavor data events in the ee channel for various p_T^{miss} bins.

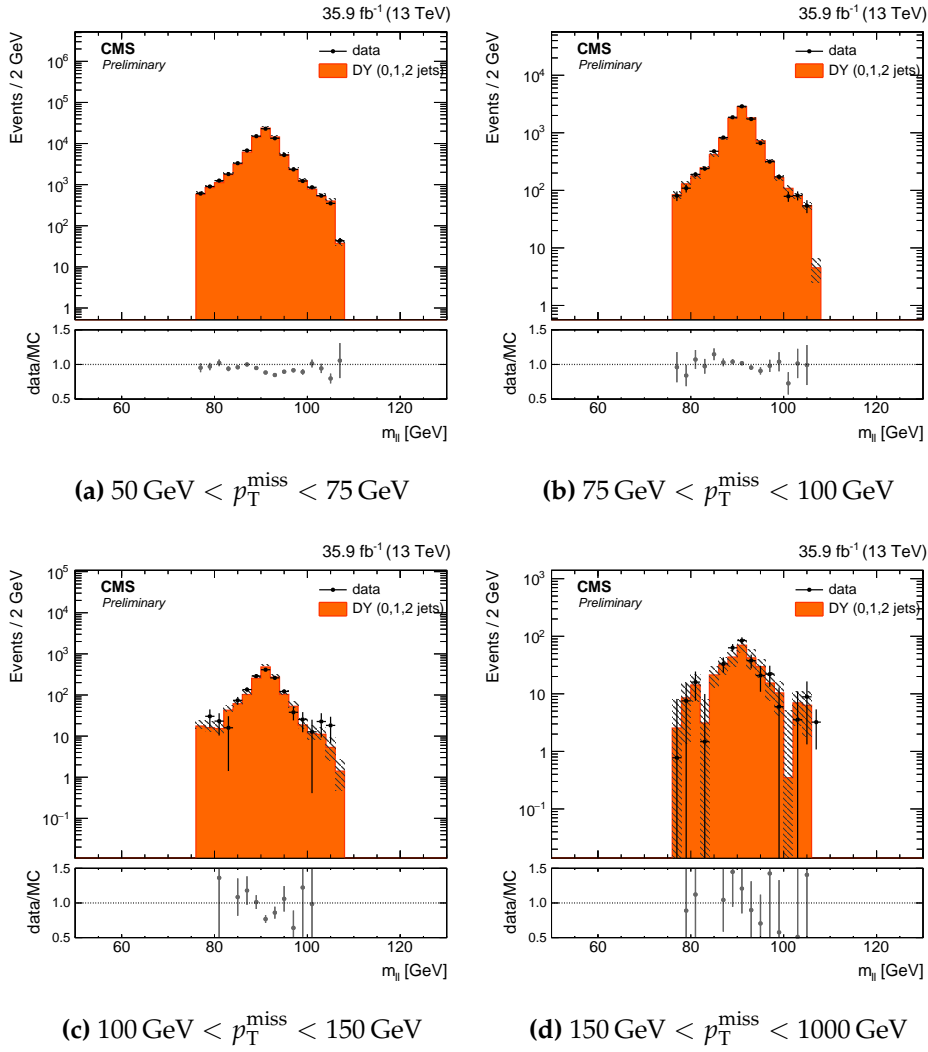


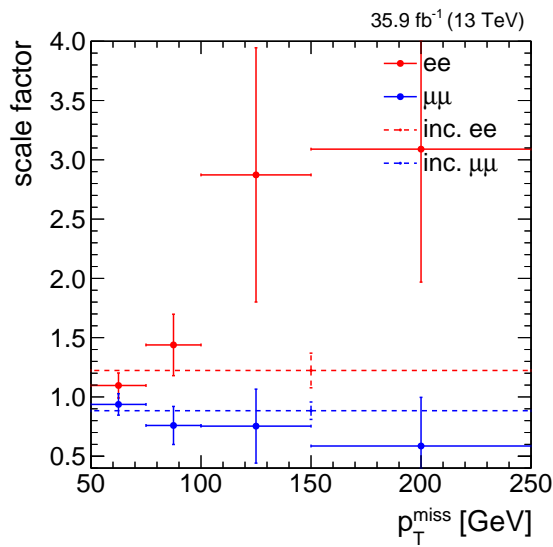
Figure 4.4.: Z peak in data and MC after subtraction of non-Drell-Yan contribution estimate from opposite-flavor data events in the $\mu\mu$ channel for various p_T^{miss} bins.

Table 4.5.: Signal region DY yields in MC and data (from $R_{\text{in/out}}$ prediction) in the ee channel

	$(N_{\text{out}}^{1b})_{\text{MC}}$	$(N_{\text{out}}^{1b})_{\text{data}}$	scale factor
$50 \text{ GeV} < p_{\text{T}}^{\text{miss}} < 75 \text{ GeV}$	623.60 ± 58.67	683.83 ± 13.85	1.10 ± 0.11
$75 \text{ GeV} < p_{\text{T}}^{\text{miss}} < 100 \text{ GeV}$	137.98 ± 22.97	198.51 ± 13.65	1.44 ± 0.26
$100 \text{ GeV} < p_{\text{T}}^{\text{miss}} < 150 \text{ GeV}$	27.61 ± 8.35	79.32 ± 17.34	2.87 ± 1.07
$150 \text{ GeV} < p_{\text{T}}^{\text{miss}} < 1000 \text{ GeV}$	17.32 ± 4.47	53.58 ± 13.66	3.09 ± 1.12

Table 4.6.: Signal region DY yields in MC and data (from $R_{\text{in/out}}$ prediction) in the $\mu\mu$ channel

	$(N_{\text{out}}^{1b})_{\text{MC}}$	$(N_{\text{out}}^{1b})_{\text{data}}$	scale factor
$50 \text{ GeV} < p_{\text{T}}^{\text{miss}} < 75 \text{ GeV}$	1444.20 ± 92.95	1353.21 ± 97.49	0.94 ± 0.091
$75 \text{ GeV} < p_{\text{T}}^{\text{miss}} < 100 \text{ GeV}$	293.68 ± 38.12	223.03 ± 37.18	0.76 ± 0.16
$100 \text{ GeV} < p_{\text{T}}^{\text{miss}} < 150 \text{ GeV}$	113.32 ± 16.96	85.42 ± 32.96	0.75 ± 0.31
$150 \text{ GeV} < p_{\text{T}}^{\text{miss}} < 1000 \text{ GeV}$	41.85 ± 9.82	24.53 ± 16.18	0.59 ± 0.41

**Figure 4.5.:** Data/MC scale factors binned in $p_{\text{T}}^{\text{miss}}$ applied to MC events used for the estimate of the Drell-Yan normalization in the dilepton channel signal regions.

4.3. $t\bar{t} + V$, diboson processes, and single top

4.4. Fake lepton background

Another type of reducible background, the fake (or non-prompt) lepton background, is also estimated using observed events. Processes which contain only one prompt electron or muon in the final state may pass the signal region selection as described in Sec. 3.4 by the jet-induced faking of a second lepton. Namely, processes such as W +jets, semileptonic decays of $t\bar{t}$ and tW associated production, and leptonic single top decays.

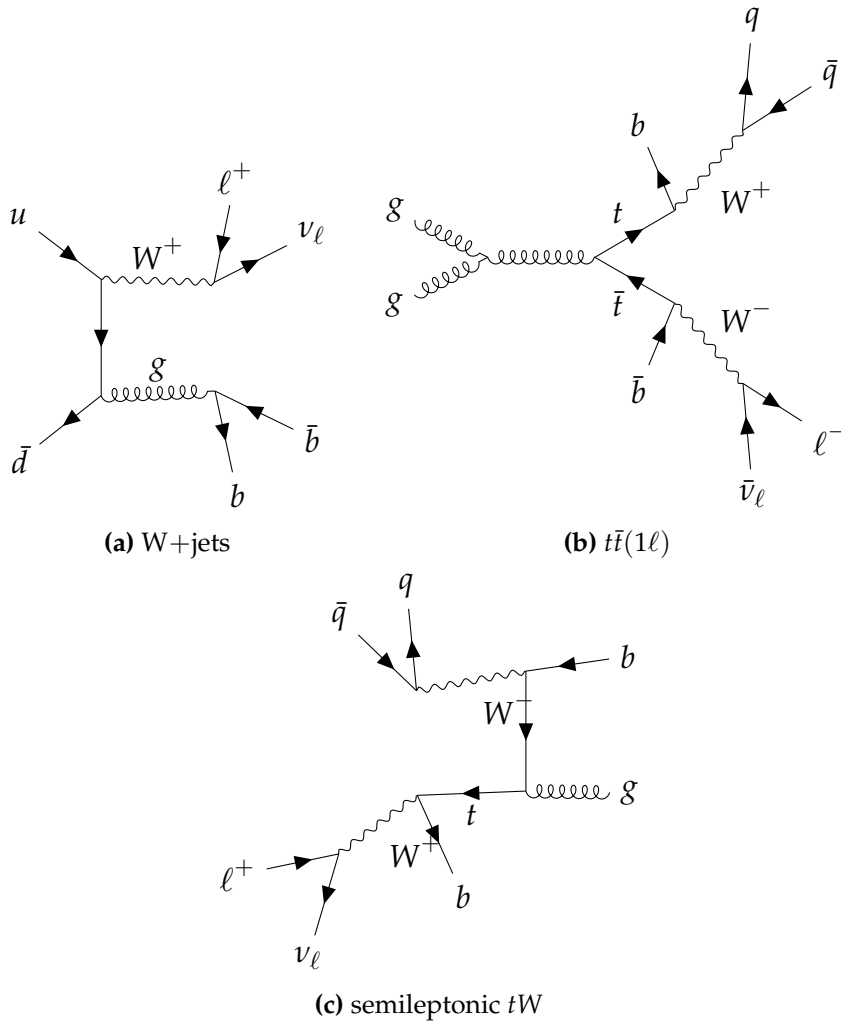


Figure 4.6.: Examples of (a) W +jets, (b) semileptonic $t\bar{t}$, and (c) semileptonic tW diagrams that contribute to the fake lepton background.

Appendix A.

Pointless extras

*“Le savant n’étudie pas la nature parce que cela est utile;
il l’étudie parce qu’il y prend plaisir,
et il y prend plaisir parce qu’elle est belle.”*

— Henri Poincaré, 1854–1912

Appendixes (or should that be “appendices”?) make you look really clever, ‘cos it’s like you had more clever stuff to say than could be fitted into the main bit of your thesis. Yeah. So everyone should have at least three of them...

A.1. Like, duh

Padding? What do you mean?

A.2. $y = \alpha x^2$

See, maths in titles automatically goes bold where it should (and check the table of contents: it *isn't* bold there!) Check the source: nothing needs to be specified to make this work. Thanks to Donald Arsenau for the teeny hack that makes this work.

Colophon

This thesis was made in L^AT_EX 2_ε using the “hepthesis” class [17].

Bibliography

- [1] G. Bertone, D. Hooper, and J. Silk, Phys. Rept. **405**, 279 (2005), hep-ph/0404175.
- [2] J. L. Feng, Ann. Rev. Astron. Astrophys. **48**, 495 (2010), 1003.0904.
- [3] T. A. Porter, R. P. Johnson, and P. W. Graham, Ann. Rev. Astron. Astrophys. **49**, 155 (2011), 1104.2836.
- [4] G. Brianti, Phys. Rept. **403-404**, 349 (2004).
- [5] CMS, JINST **3**, S08004 (2008).
- [6] C. G. Lester and D. J. Summers, Phys. Lett. **B463**, 99 (1999), hep-ph/9906349.
- [7] S. Frixione, P. Nason, and C. Oleari, JHEP **11**, 070 (2007), 0709.2092.
- [8] S. Alioli *et al.*, JHEP **06**, 043 (2010), 1002.2581.
- [9] T. Sjöstrand *et al.*, Comput. Phys. Commun. **191**, 159 (2015), 1410.3012.
- [10] S. Agostinelli *et al.*, Nuclear Instruments and Methods in Physics Research Sec. A: Accelerators, Spectrometers, Detectors and Associated Equipment **506**, 250 (2003).
- [11] M. Beneke, P. Falgari, S. Klein, and C. Schwinn, Nucl. Phys. B **855**, 695 (2012), 1109.1536.
- [12] M. Cacciari, M. Czakon, M. Mangano, A. Mitov, and P. Nason, Phys. Lett. B **710**,

612 (2012), 1111.5869.

[13] P. Bärnreuther, M. Czakon, and A. Mitov, Phys. Rev. Lett. **109**, 132001 (2012), 1204.5201.

[14] M. Czakon and A. Mitov, JHEP **12**, 054 (2012), 1207.0236.

[15] M. Czakon and A. Mitov, JHEP **01**, 080 (2013), 1210.6832.

[16] J. Alwall *et al.*, JHEP **07**, 079 (2014), 1405.0301.

[17] A. Buckley, The hepthesis \LaTeX class.

List of figures

2.1.	Cross-section view of CMS	8
2.2.	Schematic cross-section through the CMS tracker, where a single detector modules is represented by a line, and double lines signify back-to-back modules.	9
3.1.	W^+ and W^- decay to leptons and corresponding lepton neutrinos for all lepton generations.	12
3.2.	Discriminator values for the CSVv2 algorithm for an inclusive multi-jet topology, where the total number of entries in the simulation is normalized to the observed number of entries in the data.	24
3.3.	The $M_{T2}^{\ell\ell}$ distribution in data and simulation for events passing selection requirements for the $e\mu$ channel. The distribution of two example signals (scalar and pseudoscalar mediator, $m_{\phi/a} = 100$ GeV) with $m_\chi = 1$ GeV is scaled up by a factor of 200. The last bin includes overflow. Uncertainties are statistical only.	29
4.1.	Leading order $t\bar{t}$ production diagrams probed at the LHC via (a), (b) gluon fusion, and (c) quark-antiquark annihilation.	31

4.2. The Drell-Yan lepton pair-production process mediated by a virtual photon (γ^*) or Z boson at (a) $\mathcal{O}(\alpha)$ and (b),(c),(d),(e) $\mathcal{O}(\alpha\alpha_s)$	33
4.3. Z peak in data and MC after subtraction of non-Drell-Yan contribution estimate from opposite-flavor data events in the ee channel for various p_T^{miss} bins.	39
4.4. Z peak in data and MC after subtraction of non-Drell-Yan contribution estimate from opposite-flavor data events in the $\mu\mu$ channel for various p_T^{miss} bins.	40
4.5. Data/MC scale factors binned in p_T^{miss} applied to MC events used for the estimate of the Drell-Yan normalization in the dilepton channel signal regions.	41
4.6. Examples of (a) W +jets, (b) semileptonic $t\bar{t}$, and (c) semileptonic tW diagrams that contribute to the fake lepton background.	43

List of tables

3.1. Variables and thresholds that define “FO”, “Loose”, and “Tight”. “-” indicates the variable is not considered for that working point.	15
3.2. Effective areas for electron isolation PU subtraction.	18
3.3. Variables and thresholds that define “FO”, “Veto”, and “Tight” electrons. An electron is in the barrel if it has supercluster $ \eta < 1.479$, otherwise it is in the endcap.	18
3.4. Variables and thresholds that define the “Loose” PF jet ID.	21
4.1. DY yields and $R_{\text{in/out}}$ values in the ee channel, for 0 b-tag selection . .	37
4.2. DY yields and $R_{\text{in/out}}$ values in the $\mu\mu$ channel, for 0 b-tag selection . .	38
4.3. DY yields and $R_{\text{in/out}}$ values in the ee channel, for ≥ 1 b-tag selection .	38
4.4. DY yields and $R_{\text{in/out}}$ values in the $\mu\mu$ channel, for ≥ 1 b-tag selection .	38
4.5. Signal region DY yields in MC and data (from $R_{\text{in/out}}$ prediction) in the ee channel	41
4.6. Signal region DY yields in MC and data (from $R_{\text{in/out}}$ prediction) in the $\mu\mu$ channel	41